



Development of an explicit non-staggered scheme for solving three-dimensional Maxwell's equations

Tony W.H. Sheu^{a,b,c,*}, Y.W. Chung^a, J.H. Li^a, Y.C. Wang^a

^a Department of Engineering Science and Ocean Engineering, National Taiwan University, No. 1, Sec. 4, Roosevelt Road, Taipei, Taiwan, ROC

^b Center for Advanced Study in Theoretical Sciences, National Taiwan University, Taipei, Taiwan

^c Institute of Applied Mathematical Sciences, National Taiwan University, Taipei, Taiwan

ARTICLE INFO

Article history:

Received 15 April 2014

Received in revised form

28 June 2016

Accepted 6 July 2016

Available online 15 July 2016

Keywords:

Maxwell's equations

Non-staggered grids

Zero-divergence

Symplectic partitioned Runge–Kutta

Fourth-order

Dispersion relation equation

Exact and numerical phase velocities

ABSTRACT

An explicit finite-difference scheme for solving the three-dimensional Maxwell's equations in non-staggered grids is presented. We aspire to obtain time-dependent solutions of the Faraday's and Ampère's equations and predict the electric and magnetic fields within the discrete zero-divergence context (or Gauss's law). The local conservation laws in Maxwell's equations are numerically preserved using the explicit second-order accurate symplectic partitioned Runge–Kutta temporal scheme. Following the method of lines, the spatial derivative terms in the semi-discretized Faraday's and Ampère's equations are approximated theoretically to obtain a highly accurate numerical phase velocity. The proposed fourth-order accurate space-centered finite difference scheme minimizes the discrepancy between the exact and numerical phase velocities. This minimization process considerably reduces the dispersion and anisotropy errors normally associated with finite difference time-domain methods. The computational efficiency of getting the same level of accuracy at less computing time and the ability of preserving the symplectic property have been numerically demonstrated through several test problems.

© 2016 Published by Elsevier B.V.

1. Introduction

For ideal Maxwell's equations applied in a region with no charges and no currents, Gauss's law is considered as a mathematical constraint imposed on the Faraday's law and the Ampère's law. However, this physical law for magnetism is not always discretely satisfied due to various kinds of numerical error. These predicted nonzero-divergence errors in magnetic and electric flux densities introduce instability while simulating electromagnetic wave propagation by using the Maxwell's equations. Avoidance of this numerical instability is critical in the development of an effective solver for Maxwell's equations [1]. In Gauss's law, two divergence-free constraint equations can be numerically satisfied at all time when solving the Maxwell's equations in the well known Yee's staggered grid system [2]. The generalized Lagrange multiplier formulation in [3] is an alternative to retain divergence-free condition in the Maxwell's equations. A local divergence-free Maxwell's solution can be obtained as well using the discontinuous Galerkin finite

element method [4], the space–time hp-discontinuous Galerkin method [5], and the space–time discontinuous Galerkin Trefftz method [6]. In this study a scheme with the ability to render a set of divergence-free electric and magnetic field solutions is developed in non-staggered (or collocated) grids.

The methods developed for predicting electromagnetic wave propagation can be classified into the integral and differential types. The integral methods include method of moments, boundary element method, and fast multipole method. The differential methods contain finite difference, finite element, finite volume, pseudospectral, transition line matrix and multiresolution methods. Among them, the finite difference method developed in time-domain is comparatively simple and efficient [2] and it is therefore chosen in the present study.

While approximating the derivative terms using the differential methods, any form of numerical dissipation error can deteriorate the solutions. Meanwhile, time-dispersion error can lead to an erroneously predicted phase velocity or group velocity. It is therefore essential to reduce both the numerical dispersion and dissipation errors while approximating the first-order spatial derivative terms. The appropriate symplectic property preserving approximation of time derivative terms in the Faraday's and Ampère's equations is therefore required for long-term computation of Maxwell's equations.

* Corresponding author at: Department of Engineering Science and Ocean Engineering, National Taiwan University, No. 1, Sec. 4, Roosevelt Road, Taipei, Taiwan, ROC. Fax: +886 2 23929885.

E-mail address: twhsheu@ntu.edu.tw (T.W.H. Sheu).

When simulating Maxwell's equations, the accuracy of the solution predicted from the Finite Difference Time Domain (FDTD) methods may become questionable in large and small-scale structures after the computation is executed for a long time [7]. The predicted errors manifest themselves as numerical damping and dispersion errors. The decreasing of numerical accuracy can be also attributed to the anisotropy error. Both of the dispersion and anisotropy errors are significant since they exhibit accumulative nature and therefore entail an erroneous propagation characteristics. Consequently, the resulting amplitude and phase errors will result in erroneous numerical prediction. Both of these computational issues in electro-magnetism are addressed in the current paper via the newly developed FDTD scheme for two and three dimensions.

This paper is organized as follows. In Section 2, some of the distinguished features in the Maxwell's equations are presented. In Section 3, the approximation of the first-order spatial derivative terms in the Faraday's and Ampère's equations are rigorously derived by requiring that the difference between the exact and numerical phase velocities be minimized. Since Maxwell's equations subjected to the lossless condition are Hamiltonian [8], a symplectic structure-preserving time integrator is applied in this study to conserve symplecticity in the differential equations by using the explicit Symplectic Partitioned Runge–Kutta (SPRK) scheme. In Section 4, the proposed scheme is analyzed in detail in Fourier space for completeness. In Section 5, the proposed temporal and spatial schemes are verified and validated by the chosen test problems. Finally, we will draw conclusions based on the solutions computed on the non-staggered grids.

2. Working equations

Maxwell's equations in time domain for electric field $\underline{E} = (E_x, E_y, E_z)^T$ and magnetic field $\underline{H} = (H_x, H_y, H_z)^T$ can be written in curl operator form as

$$\frac{\partial \underline{H}}{\partial t} = -\frac{1}{\mu} \nabla \times \underline{E}, \quad (1)$$

$$\frac{\partial \underline{E}}{\partial t} = \frac{1}{\varepsilon} \nabla \times \underline{H}. \quad (2)$$

For a linear, isotropic, and lossless material, in the absence of electric current density and electric charge density for all time, the Gauss's law comprising of the divergence-free constraint equations $\nabla \cdot \underline{B} = 0$ and $\nabla \cdot \underline{D} = 0$ can be directly derived from Eqs. (1)–(2), which denote the Faraday's law and the Ampère's law, respectively. The Gauss's law fixes the initial conditions for Eqs. (1) and (2) and it is always satisfied within the differential context if both vectors \underline{B} and \underline{D} are initially divergence-free [4]. Note that Eqs. (1)–(2) are derived by using the constitutive equations $\underline{D} = \varepsilon \underline{E}$ and $\underline{B} = \mu \underline{H}$, where $\varepsilon = \varepsilon_0 \varepsilon_r$ and $\mu = \mu_0 \mu_r$. The subscript “r” shown in the permittivity and permeability denotes the quantities in free space. ε_r and μ_r stand for the relative permittivity and permeability, respectively. In these constitutive equations, the electric flux density \underline{D} is linearly proportional to the electric field density \underline{E} , where the proportional constant ε is known as the electric permittivity. Likewise, the magnetic flux density \underline{B} relates with the magnetic field intensity \underline{H} through the proportional constant μ known as the magnetic permeability. The values of ε_0 and μ_0 at vacuum state define the light speed $c \equiv (\varepsilon_0 \mu_0)^{-1/2}$. These constitutive equations and the Ampère and Faraday equations constitute twelve equations for twelve unknowns \underline{B} , \underline{D} , \underline{H} and \underline{E} . In this study, the schemes proposed in Section 3 for Maxwell's equations are rather restrictive in a sense that they can be applied only to a homogeneous isotropic material.

Eqs. (1)–(2) constitute a bi-Hamiltonian differential system containing two frequently referred Hamiltonians, namely the helicity Hamiltonian H_1 given below [9]

$$H_1 = \frac{1}{2} \int \frac{1}{\varepsilon} \underline{H} \cdot \nabla \times \underline{H} + \frac{1}{\mu} \underline{E} \cdot \nabla \times \underline{E} d\Omega \quad (3)$$

and the quadratic Hamiltonian given below [10]

$$H_2 = \frac{1}{2} \int \mu \underline{H} \cdot \underline{H} + \varepsilon \underline{E} \cdot \underline{E} d\Omega. \quad (4)$$

Note that Eqs. (1)–(2) permit not only the global conservation law given by $\frac{dH_1}{dt} = 0$ but also the quadratic conservation law represented as $\frac{dH_2}{dt} = 0$ provided that electric permittivity and magnetic permeability are independent of the spatial variables [11].

3. Numerical method

Maxwell's equations in simple media have symplectic and multisymplectic structures. Preservation of these invariant properties prompts us to apply a geometric numerical integration method in order to satisfy energy conservation law in discrete form and gauge invariant existing in the Maxwell's equations [12].

Following the method of lines, the Hamiltonian system of equations under current investigation shall be discretized in space by using a centered finite difference scheme. The symplectic method is then applied to discretize the resulting ordinary differential equations in time. In this paper, preservation of the local and global conservation laws and the discrete divergence-free (or Gauss) law will be addressed. To get some numerical insights of the proposed scheme, both of the dispersion analysis and the modified equation analysis will be performed. Anisotropy analysis will be also conducted on the proposed symplectic scheme. Discussion of results is particularly focused on the grid-anisotropy for the equations $\frac{\partial H_x}{\partial t} = -\frac{1}{\mu} \frac{\partial E_z}{\partial y}$, $\frac{\partial H_y}{\partial t} = \frac{1}{\mu} \frac{\partial E_z}{\partial x}$ and $\frac{\partial E_z}{\partial t} = \frac{1}{\varepsilon} \left(\frac{\partial H_y}{\partial x} - \frac{\partial H_x}{\partial y} \right)$.

In 1960, Yee first solved the Maxwell's equations on staggered grids [2]. While the strategy of storing the electric and magnetic field variables at different nodal points makes the boundary treatment a comparatively easy task and satisfies the Gauss's law in the discrete level, a more stringent condition is required for numerical stability. On the contrary, within the context of finite difference methods, very few non-staggered Maxwell's equation solvers have been proposed with success to accurately predict the EM wave solutions in the literature [13–15]. Dependent variables can be also stored in a space–time fashion in discontinuous Galerkin time domain methods [5,6]. Basis functions can be properly designed by exploiting the geometric structure behind the Maxwell's equations [16]. In the current study, the non-staggered grid finite difference approach is adopted. The reason for choosing collocated grid approach is due to its simplicity in programming and storage management.

3.1. Explicit symplectic partitioned Runge–Kutta temporal scheme

Faraday's and Ampère's equations shown in (1)–(2) constitute a Hamiltonian differential system. Apart from preserving the symplectic structure along the time direction, we also aim to develop a scheme of reduced dispersion error. To this end, the difference between the numerical and exact phase velocities will be minimized in wavenumber space.

Most of the Hamiltonian systems have a special structure called separable. Since Maxwell's equations are separable, an explicit symplectic partitioned Runge–Kutta time-stepping scheme (or Verlet scheme) is therefore applied to integrate the differential

system of equations through the corresponding table for the respective Faraday's and Ampère's equations [17]. In this study, the following second-order accurate explicit partitioned Runge–Kutta scheme presented in [18] is adopted to approximate the time derivative terms

$$\underline{H}^{n+\frac{1}{2}} = \underline{H}^n - \frac{dt}{2\mu} \nabla \times \underline{E}^n, \tag{5}$$

$$\underline{E}^{n+1} = \underline{E}^n + \frac{dt}{\varepsilon} \nabla \times \underline{H}^{n+\frac{1}{2}}, \tag{6}$$

$$\underline{H}^{n+1} = \underline{H}^{n+\frac{1}{2}} - \frac{dt}{2\mu} \nabla \times \underline{E}^{n+1}. \tag{7}$$

Note that the above temporal scheme is numerically identical to the Yee's leap-frog scheme except for that outlined in the very first half time step.

3.2. Discretization of spatial derivative terms

Approximation of the spatial derivative terms shown in Eqs. (5)–(7) is presented below by using the modified equation analysis given in Section 3.2.1, dispersion analysis given in Section 3.2.2, and the grid-anisotropy analysis presented in Section 4.2.

In non-staggered grids, the first-order derivative terms $\frac{\partial H_y^n}{\partial x}$ and $\frac{\partial H_x^n}{\partial y}$ at an interior node (i, j, k) are approximated by the difference scheme given below

$$\frac{\partial H_y}{\partial x} \Big|_{i,j,k}^n = \frac{1}{h} \left[a_1 (H_y|_{i+3,j,k}^n - H_y|_{i-3,j,k}^n) + a_2 (H_y|_{i+2,j,k}^n - H_y|_{i-2,j,k}^n) + a_3 (H_y|_{i+1,j,k}^n - H_y|_{i-1,j,k}^n) \right], \tag{8}$$

$$\frac{\partial H_x}{\partial y} \Big|_{i,j,k}^n = \frac{1}{h} \left[a_1 (H_x|_{i,j+3,k}^n - H_x|_{i,j-3,k}^n) + a_2 (H_x|_{i,j+2,k}^n - H_x|_{i,j-2,k}^n) + a_3 (H_x|_{i,j+1,k}^n - H_x|_{i,j-1,k}^n) \right]. \tag{9}$$

Upon the substitution of Eqs. (8), (9) into the equation for $E_z^{n+1/2}$, we perform Taylor series expansion with respect to E_z . The following equation at an interior point (i, j, k) can be derived

$$\begin{aligned} & \frac{\partial E_z}{\partial t} \Big|_{i,j,k}^n + \frac{dt^2}{24} \frac{\partial^3 E_z}{\partial t^3} \Big|_{i,j,k}^n + \frac{dt^4}{1920} \frac{\partial^5 E_z}{\partial t^5} \Big|_{i,j,k}^n \\ & + \frac{dt^6}{322560} \frac{\partial^7 E_z}{\partial t^7} \Big|_{i,j,k}^n + \dots \\ & = \frac{1}{\varepsilon} \left\{ \left[(6a_1 + 4a_2 + 2a_3) \frac{\partial H_y}{\partial x} \Big|_{i,j,k}^n \right. \right. \\ & + \left(9a_1 + \frac{8}{3}a_2 + \frac{1}{3}a_3 \right) dx^2 \frac{\partial^3 H_y}{\partial x^3} \Big|_{i,j,k}^n \\ & + \left(\frac{81}{20}a_1 + \frac{8}{15}a_2 + \frac{1}{60}a_3 \right) dx^4 \frac{\partial^5 H_y}{\partial x^5} \Big|_{i,j,k}^n \\ & + \left(\frac{243}{280}a_1 + \frac{16}{315}a_2 + \frac{1}{2520}a_3 \right) dx^6 \frac{\partial^7 H_y}{\partial x^7} \Big|_{i,j,k}^n \\ & + \dots \left. \right] - \left[(6a_1 + 4a_2 + 2a_3) \frac{\partial H_y}{\partial x} \Big|_{i,j,k}^n \right. \\ & + \left(9a_1 + \frac{8}{3}a_2 + \frac{1}{3}a_3 \right) dx^2 \frac{\partial^3 H_y}{\partial x^3} \Big|_{i,j,k}^n \end{aligned}$$

$$\left. + \left(\frac{81}{20}a_1 + \frac{8}{15}a_2 + \frac{1}{60}a_3 \right) dx^4 \frac{\partial^5 H_y}{\partial x^5} \Big|_{i,j,k}^n + \left(\frac{243}{280}a_1 + \frac{16}{315}a_2 + \frac{1}{2520}a_3 \right) dx^6 \frac{\partial^7 H_y}{\partial x^7} \Big|_{i,j,k}^n + \dots \right\}. \tag{10}$$

The weighting coefficients a_1 , a_2 and a_3 will be determined by the modified equation analysis and the dispersion analysis given below.

3.2.1. Modified equation analysis

Higher order temporal terms $\frac{\partial^3 E_z}{\partial t^3}, \frac{\partial^5 E_z}{\partial t^5}, \frac{\partial^7 E_z}{\partial t^7} \dots$ are rewritten to their equivalent spatial derivative terms through the Ampère's equations $\frac{\partial E_z}{\partial t} = \frac{1}{\varepsilon} \left(\frac{\partial H_y}{\partial x} - \frac{\partial H_x}{\partial y} \right), \frac{\partial E_x}{\partial t} = \frac{1}{\varepsilon} \left(\frac{\partial H_z}{\partial y} - \frac{\partial H_y}{\partial z} \right),$ and $\frac{\partial E_y}{\partial t} = \frac{1}{\varepsilon} \left(\frac{\partial H_x}{\partial z} - \frac{\partial H_z}{\partial x} \right)$ to yield the corresponding equations for $\frac{\partial^i E_j}{\partial t^i}$ ($i = 3$ and $5, j = x, y, z$). By replacing the temporal derivative terms $\frac{\partial^3 E_z}{\partial t^3}$ and $\frac{\partial^5 E_z}{\partial t^5}$ with the spatial derivative terms, one can get the corresponding equation for (10). In comparison with the equation $\frac{\partial E_z}{\partial t} = \frac{1}{\varepsilon} \left(\frac{\partial H_y}{\partial x} - \frac{\partial H_x}{\partial y} \right),$ the following algebraic equations for a_1, a_2 and a_3 can be derived

$$3a_1 + 2a_2 + a_3 = \frac{1}{2}, \tag{11}$$

and

$$9a_1 + \frac{8}{3}a_2 + \frac{1}{3}a_3 - \frac{Cr^2}{12}(3a_1 + 2a_2 + a_3) = 0. \tag{12}$$

In the above, the Courant number is defined by $Cr = \frac{c\Delta t}{h}$ and h denotes the grid spacing. The algebraic equations for $E_x^{n+1/2}$ and $E_y^{n+1/2}$ can be similarly derived.

3.2.2. Dispersion analysis

Determination of the three introduced weighting coefficients requires the third algebraic equation. In this study, the dispersion analysis detailed in [19] is adopted to get the numerical dispersion relation equation of the proposed scheme. By applying the curl operator on both sides of the Faraday's equations and substituting the resulting equations into the Ampère's equations, one can get the second-order wave equation for \underline{E} , which is $\frac{1}{c^2} \frac{\partial^2 \underline{E}}{\partial t^2} = \frac{\partial^2 \underline{E}}{\partial x^2} + \frac{\partial^2 \underline{E}}{\partial y^2} + \frac{\partial^2 \underline{E}}{\partial z^2}$. Next, using the plane wave solution $\underline{E} = E_0 \exp(I(k_x i \Delta x + k_y j \Delta y + k_z k \Delta z - \omega n \Delta t))$, where $I = \sqrt{-1}$, it is seen that

$$\frac{\partial^2 \underline{E}}{\partial t^2} = 4 \left(\frac{2 \sin \left(\frac{\omega \Delta t}{2} \right)}{\Delta t} \right)^2 \underline{E}, \tag{13}$$

$$\frac{\partial^2 \underline{E}}{\partial x^2} = -4 \left(\frac{a_1 \sin(3k_x \Delta x) + a_2 \sin(2k_x \Delta x) + a_3 \sin(k_x \Delta x)}{\Delta x} \right)^2 \underline{E}, \tag{14}$$

$$\frac{\partial^2 \underline{E}}{\partial y^2} = -4 \left(\frac{a_1 \sin(3k_y \Delta y) + a_2 \sin(2k_y \Delta y) + a_3 \sin(k_y \Delta y)}{\Delta y} \right)^2 \underline{E}, \tag{15}$$

$$\frac{\partial^2 \underline{E}}{\partial z^2} = -4 \left(\frac{a_1 \sin(3k_z \Delta z) + a_2 \sin(2k_z \Delta z) + a_3 \sin(k_z \Delta z)}{\Delta z} \right)^2 \underline{E}. \tag{16}$$

Finally, the following numerical dispersion relation equation can be derived by substituting all the relations in Eqs. (13)–(16) into the second-order wave equation for \underline{E}

$$\begin{aligned} & \frac{1}{c^2} \frac{\sin^2(\omega \Delta t / 2)}{\Delta t^2} \\ &= \left(\frac{a_1 \sin(3k_x \Delta x) + a_2 \sin(2k_x \Delta x) + a_3 \sin(k_x \Delta x)}{\Delta x} \right)^2 \\ &+ \left(\frac{a_1 \sin(3k_y \Delta y) + a_2 \sin(2k_y \Delta y) + a_3 \sin(k_y \Delta y)}{\Delta y} \right)^2 \\ &+ \left(\frac{a_1 \sin(3k_z \Delta z) + a_2 \sin(2k_z \Delta z) + a_3 \sin(k_z \Delta z)}{\Delta z} \right)^2. \quad (17) \end{aligned}$$

The exact dispersion relation equation is derived by substituting the plane wave solution into the second-order wave equation $\frac{\partial^2 \underline{E}}{\partial t^2} = c^2 \nabla^2 \underline{E}$, thereby yielding $(\frac{\omega}{c})^2 = k_x^2 + k_y^2 + k_z^2$. Note that the wavenumber vector is defined as $\underline{k} = (k_x, k_y, k_z)$.

Next, the consistency analysis is conducted from the above derived numerical dispersion relation equation, which can be rewritten as follows

$$\begin{aligned} & \frac{1}{c^2} \frac{\omega^2}{4} \left(\frac{\sin(\omega \Delta t / 2)}{\omega \Delta t} \right)^2 \\ &= k_x^2 \left(3a_1 \frac{\sin(3k_x \Delta x)}{3k_x \Delta x} + 2a_2 \frac{\sin(2k_x \Delta x)}{2k_x \Delta x} + a_3 \frac{\sin(k_x \Delta x)}{k_x \Delta x} \right)^2 \\ &+ k_y^2 \left(3a_1 \frac{\sin(3k_y \Delta y)}{3k_y \Delta y} + 2a_2 \frac{\sin(2k_y \Delta y)}{2k_y \Delta y} + a_3 \frac{\sin(k_y \Delta y)}{k_y \Delta y} \right)^2 \\ &+ k_z^2 \left(3a_1 \frac{\sin(3k_z \Delta z)}{3k_z \Delta z} + 2a_2 \frac{\sin(2k_z \Delta z)}{2k_z \Delta z} \right. \\ &\quad \left. + a_3 \frac{\sin(k_z \Delta z)}{k_z \Delta z} \right)^2. \quad (18) \end{aligned}$$

As Δt , Δx , Δy and Δz approach zero, Eq. (18) becomes $\frac{\omega^2}{4c^2} = (3a_1 + 2a_2 + a_3)^2 k_x^2 + (3a_1 + 2a_2 + a_3)^2 k_y^2 + (3a_1 + 2a_2 + a_3)^2 k_z^2$. Thanks to the equation derived from the modified equation analysis of second kind, the numerical and exact dispersion relation equations are identical.

To get an accurate propagation characteristics while solving the Maxwell's equations, it is essential to reduce numerical dispersion error. Numerical dispersion relation equation relates the derived numerical angular frequency ω with the wavenumber vector \underline{k} for the Maxwell's equations. A higher dispersion accuracy can be obtained provided that the numerical angular frequency of the system of Ampère's and Faraday's equations has a good match with the wavenumber. Our strategy of deriving the last algebraic equation is to develop a scheme whose numerical phase velocity agrees perfectly with its exact counterpart. To achieve this goal, the equation in space–time domain (\underline{x}, t) is transformed to its corresponding wavenumber–angular frequency space (\underline{k}, ω) .

In contrast to the numerical viewpoint of deriving the dispersion relation equation by directly relating the numerical angular frequency with the modified wavenumber, the physical viewpoint of minimizing the dispersion error is emphasized here. Phase velocity \underline{v}_p ($\equiv \frac{\omega_{num}}{\underline{k}}$) and group velocity \underline{v}_g ($\equiv \frac{\partial \omega_{num}}{\partial \underline{k}}$) are the two most important physical quantities relevant to the above derived numerical/exact dispersion relation equations. Phase velocity denotes the velocity at which the phase of a wave propagates along the direction normal to the propagating wavefront. The group velocity stands for the velocity at which the envelop of wave packet propagates in the direction normal to the constant ω -surface of the dispersion relation [20].

Table 1

Comparison of the L_2 -error norms at $t = 10$ for the component E_z obtained at different integration parameters m in a domain of 201^2 mesh points.

Parameter m	L_2 -error norm of E_z
1/2	2.2340E–04
3/7	5.5748E–04
2/5	3.5673E–04
1/3	6.1732E–04

According to the derived numerical dispersion relation equation (17) or (18), the associated numerical group velocity magnitude depends on the wavenumber vector \underline{k} . In this study the difference between the exact phase velocity and the numerical phase velocity shall be minimized. Following this line of thought, we define first the error function as $\left[\left| \frac{\omega_{num}}{\underline{k}} \right| - \left| \frac{\omega_{exact}}{\underline{k}} \right| \right]^2$. This error function is then minimized in a weak sense within the integral range of $-m_p \pi \leq h \underline{k} \leq m_p \pi$

$$E_p = \int_{-m_p \pi}^{m_p \pi} \left[\left| \frac{\omega_{num}}{\underline{k}} \right| - \left| \frac{\omega_{exact}}{\underline{k}} \right| \right]^2 W_p d(k_x \Delta x) d(k_y \Delta y) d(k_z \Delta z). \quad (19)$$

In the above, $k_x \Delta x$, $k_y \Delta y$ and $k_z \Delta z$ denote the scaled (or modified) wavenumbers along the x , y and z directions, respectively. Introduction of the weighting function W_p to the above minimization procedure enables us to integrate the equation for E_p analytically. The parameter m_p ranging from 0 to 0.5 is included to reduce the aliasing error.

The value of E_p is minimized, or $\min(E_p)$, by enforcing the limiting condition given by $\frac{\partial E_p}{\partial a_3} = 0$. The third algebraic equation for a_1 , a_2 and a_3 can thus be derived as follows

$$\begin{aligned} & -0.00946472 a_1 - 0.00787899 a_2 + 0.224744 a_1^3 \\ &+ 0.0948775 a_2^3 + 0.367829 a_2^2 a_1 \\ &+ 0.0166091 a_3^3 + 0.107206 a_3^2 a_1 + 0.261056 a_1^2 a_3 \\ &+ 0.156637 a_2^2 a_3 - 0.00453852 a_3 \\ &+ 0.492672 a_1^2 a_2 + 0.395351 a_3 a_2 a_1 + 0.0875208 a_3^2 a_2 = 0. \quad (20) \end{aligned}$$

Eq. (20) derived by minimizing the dispersion error is used together with the other two algebraic equations (11) and (12) derived previously from the modified equation analysis of second kind. From the simulation results tabulated in Table 1, the best result is obtained at $m_p = \frac{1}{2}$. Hence the three introduced coefficients in Eqs. (8)–(9) are $a_1 = 0.0164892$, $a_2 = -0.1484569$ and $a_3 = 0.74744617$. The resulting space-centered finite difference scheme is shown to have the spatial accuracy order of four since $\frac{\partial H_x}{\partial x} = \frac{\partial H_x}{\partial x} |_{exact} - 0.018459 h^4 \frac{\partial^5 H_x}{\partial x^5} + O(h^6) + \dots$.

Before conducting the fundamental studies on the proposed phase velocity optimized scheme, the derived order of accuracy, the weighting coefficients, the leading error terms in the modified equation of second kind, and the best integration parameter m_p are summarized in Table 2.

4. Fundamental analyses

The details of the proposed symplecticity-preserving scheme endowed with the optimized numerical phase velocity for Maxwell's equations are explored through the Von Neumann stability analysis given in Section 4.1 and the anisotropy analysis given in Section 4.2.

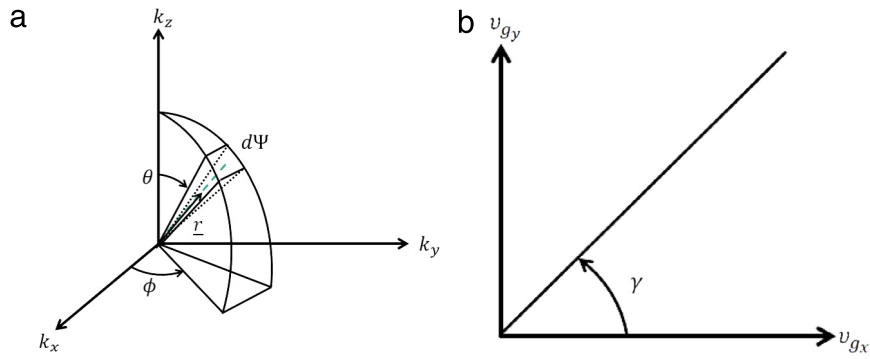


Fig. 1. (a) Schematic of a wave propagating along a direction defined by the zenith angle θ and the azimuthal angle ϕ . $d\Psi (= \sin \theta d\theta d\phi)$ denotes the differential solid angle for a wave along the direction \vec{r} ; (b) Definition of the group velocity angle γ at $k_z = 0$.

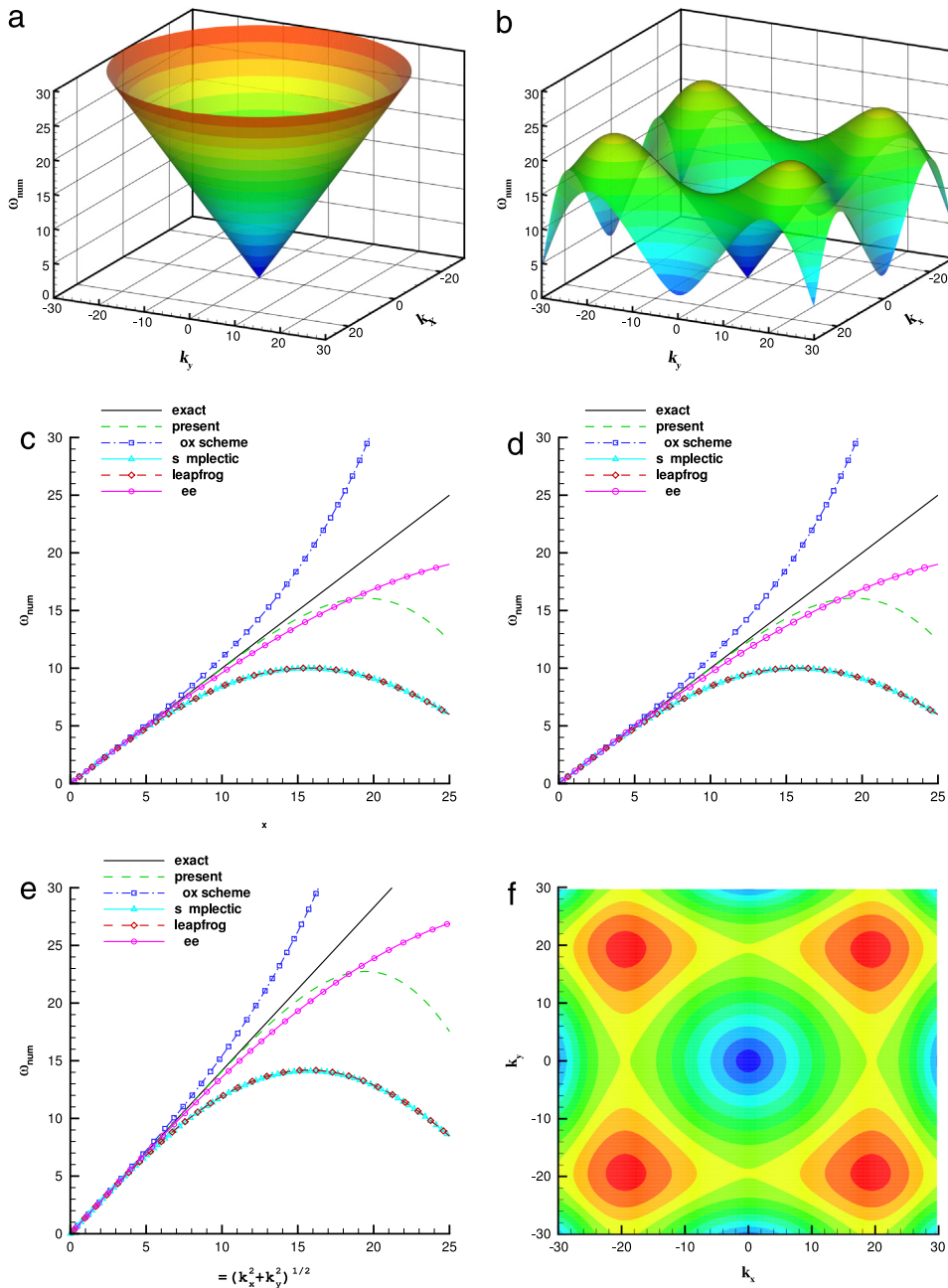


Fig. 2. The exact (a) and the numerical (b) angular frequencies are plotted with respect to k_x and k_y in $\vec{k} = (k_x, k_y)$ at $\Delta t = 0.01$, $\Delta x = \Delta y = 0.1$; (c) the plot of ω_{num} with respect to k_x for $k_y = 0$; (d) the plot of ω_{num} with respect to k_y for $k_x = 0$; (e) the plot of ω_{num} with respect to $|\vec{k}|$; (f) the contours of numerical angular frequency.

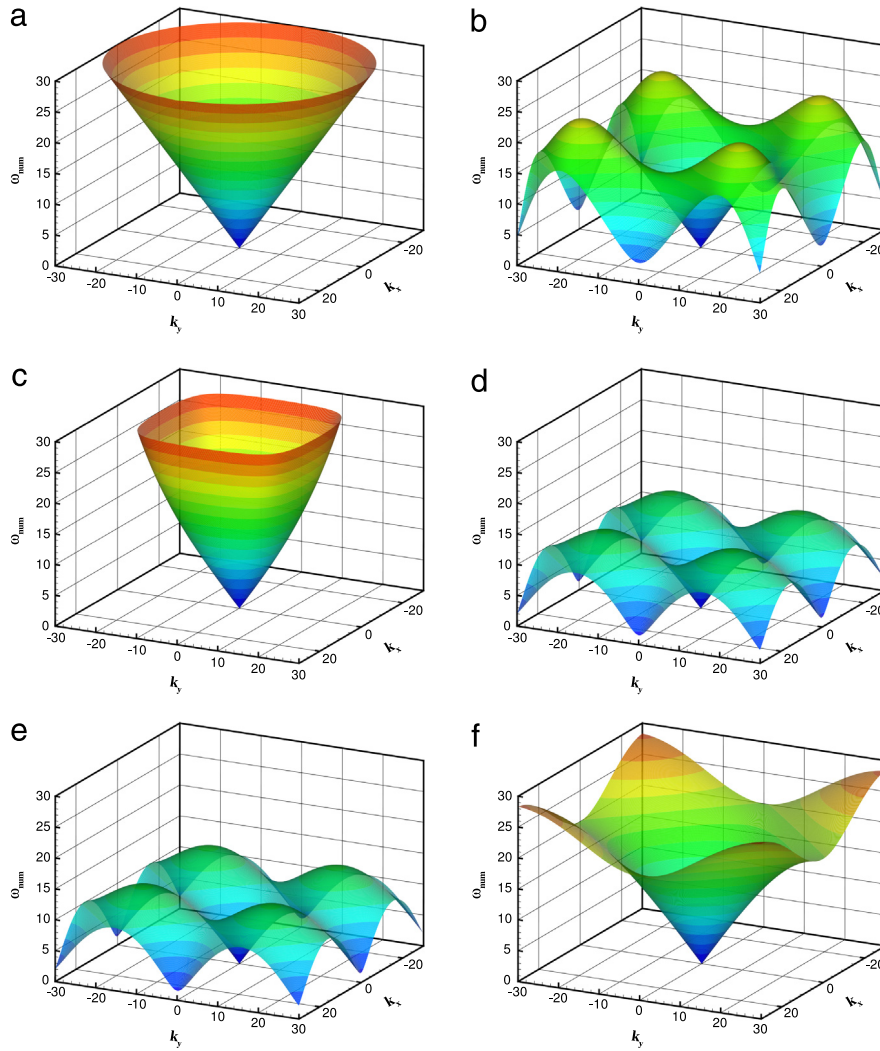


Fig. 3. Angular frequencies are plotted with respect to the wave numbers k_x and k_y . (a) Exact; (b) present numerical phase velocity optimized scheme; (c) box scheme [11]; (d) symplectic scheme [11]; (e) Leapfrog scheme [11]; (f) Yee's scheme [2].

Table 2

Summary of the characteristics of the derived optimized scheme for $\frac{\partial H_x}{\partial x}$ by minimizing the error between the exact and numerical phase velocities.

Minimization target	Parameter m_p	Accuracy order	Coefficient of the leading error term in the modified equation of 2nd kind	a_1, a_2 and a_3 in (13)
Phase velocity	$\frac{1}{2}$	4	-0.018459	$a_1 = 0.0164892$ $a_2 = -0.1484569$ $a_3 = 0.74744617$

4.1. Stability analysis

The derivation of the stability condition for the proposed explicit scheme is initiated with the scaling of field variables by $\underline{E} = \sqrt{\frac{1}{\epsilon}} \underline{E}^*$ and $\underline{H} = \sqrt{\frac{1}{\mu}} \underline{H}^*$. We then rewrite Eqs. (1)–(2) for $\underline{V} = \underline{H}^* + I \underline{E}^*$ in the normalized space as follows with the superscript “*” being omitted for the sake of simplicity.

$$\frac{1}{c} \frac{\partial \underline{V}}{\partial t} = I \nabla \times \underline{V}. \quad (21)$$

Following the work of Taflove and Brodwin [23], the stability condition for (21) using the proposed symplecticity and dispersion relation preserving explicit scheme is derived by considering the

following two equivalent eigenvalue equations

$$\frac{\partial \underline{V}}{\partial t} = \lambda \underline{V}, \quad (22)$$

$$Ic \nabla \times \underline{V} = \lambda \underline{V}. \quad (23)$$

Eq. (22) is approximated as $\underline{V}^{n+\frac{1}{2}} - \underline{V}^{n-\frac{1}{2}} = \lambda \Delta t \underline{V}^n$ using the temporal scheme described in Section 3.1. The amplification factor is defined as $G = \left| \frac{\underline{V}^{n+\frac{1}{2}}}{\underline{V}^n} \right|$. One can then easily derive the equation $G^2 - (\lambda \Delta t) G - 1 = 0$ to get the values of $G_{1,2} = \frac{\lambda \Delta t}{2} \pm \left(1 + \left(\frac{\lambda \Delta t}{2} \right)^2 \right)^{\frac{1}{2}}$. The explicit scheme is conditionally stable provided that $\text{Re}(\lambda) = 0$, thereby leading to $|\text{Im}(\lambda)| \leq \frac{2}{\Delta t}$.

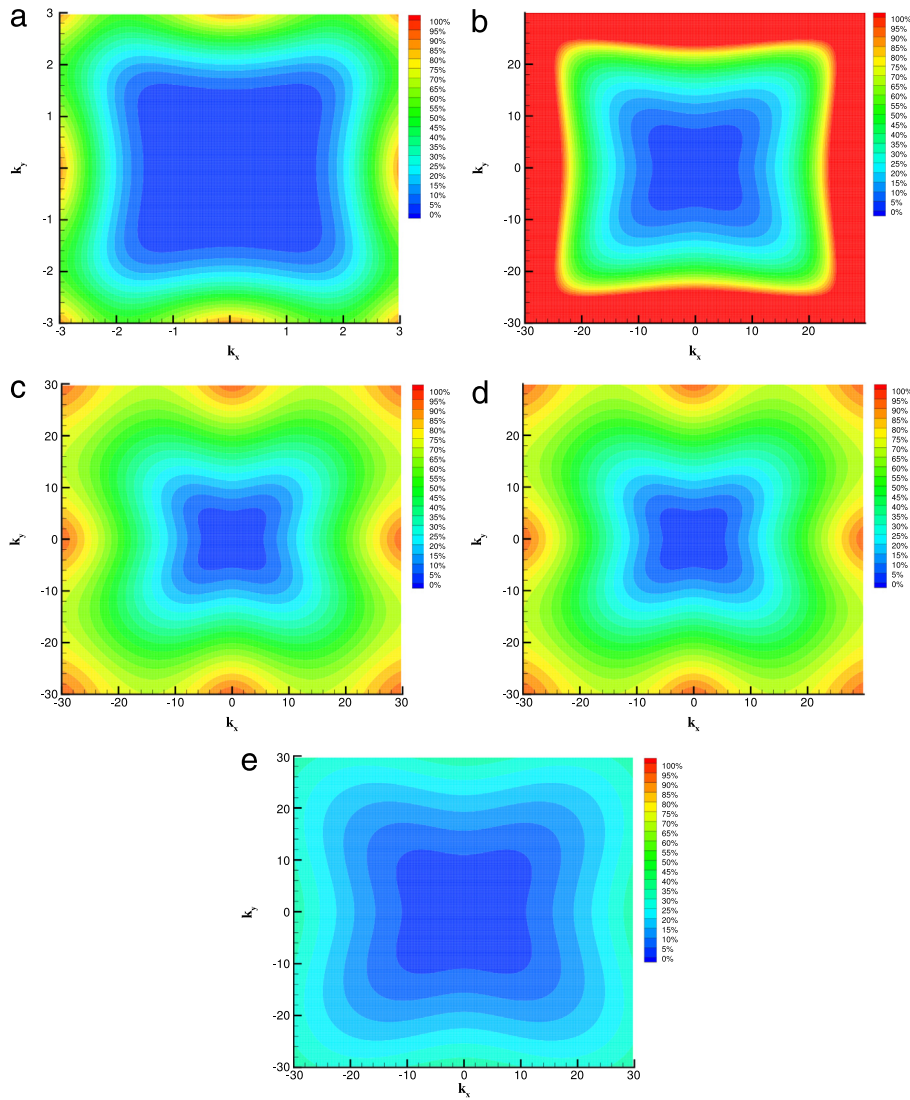


Fig. 4. The contours of $\frac{(\omega_{num} - \omega_{exact})}{\omega_{exact}} \times 100\%$ are plotted with respect to k_x and k_y among the five investigated schemes. (a) The present phase velocity optimized scheme; (b) box scheme [11]; (c) symplectic scheme [11]; (d) Leapfrog scheme [11]; (e) Yee's scheme [2].

Substitution of the equation $\frac{\partial \underline{V}}{\partial t} = \lambda \underline{V}$ into (23) yields $\frac{1}{c} \frac{\partial \underline{V}}{\partial t} = I \nabla \times \underline{V}$ or $v \left(\frac{\partial V_z}{\partial y} - \frac{\partial V_y}{\partial z} \right) = \lambda V_x$, $v \left(\frac{\partial V_x}{\partial z} - \frac{\partial V_z}{\partial x} \right) = \lambda V_y$, and $v \left(\frac{\partial V_y}{\partial x} - \frac{\partial V_x}{\partial y} \right) = \lambda V_z$. These equations can be recast into the matrix equation $\underline{F} \underline{V} = 0$, where

$$\underline{F} = \begin{pmatrix} -\lambda & -2c \frac{F_z}{\Delta z} & 2c \frac{F_y}{\Delta y} \\ 2c \frac{F_z}{\Delta z} & -\lambda & -2c \frac{F_x}{\Delta x} \\ -2c \frac{F_y}{\Delta y} & 2c \frac{F_x}{\Delta x} & -\lambda \end{pmatrix}. \quad (24)$$

In the above, $F_x = a_1 \sin(3k_x \Delta x) + a_2 \sin(2k_x \Delta x) + a_3 \sin(k_x \Delta x)$, $F_y = a_1 \sin(3k_y \Delta y) + a_2 \sin(2k_y \Delta y) + a_3 \sin(k_y \Delta y)$, and $F_z = a_1 \sin(3k_z \Delta z) + a_2 \sin(2k_z \Delta z) + a_3 \sin(k_z \Delta z)$. The unique solution \underline{V} is obtained from $\underline{F} \underline{V} = 0$, provided that the determinant of \underline{F} is equal to zero, thereby leading to $\lambda^2 = -4c^2 \left(\frac{F_x^2}{\Delta x^2} + \frac{F_y^2}{\Delta y^2} \right)$. For all the possible wavenumbers k_x , k_y and k_z , the condition,

i.e. $\text{Re}(\lambda) = 0$, is necessary in order to get the stability condition given by $|\text{Im}(\lambda)| \leq 2c \left(\frac{\max(F_x^2)}{\Delta x^2} + \frac{\max(F_y^2)}{\Delta y^2} + \frac{\max(F_z^2)}{\Delta z^2} \right)^{\frac{1}{2}}$.

Subjected to the constraint equation given by $|\text{Im}(\lambda)| \leq \frac{2}{\Delta t}$, the convergent solution is sought under the condition of $\Delta t \leq \frac{1}{c} \left(\frac{\max(F_x^2)}{\Delta x^2} + \frac{\max(F_y^2)}{\Delta y^2} + \frac{\max(F_z^2)}{\Delta z^2} \right)^{-\frac{1}{2}}$. By plugging the previously derived coefficients a_1 , a_2 and a_3 into the above inequality equation, the stability condition, $\Delta t \leq 0.673844 \frac{h}{c}$ for the conditionally stable explicit scheme for the three-dimensional Maxwell's equations is derived. Through this Von-Neumann stability analysis, the maximum allowable Δt of the present scheme is larger than that of the Yee's scheme. Subjected to the stability condition and the consistency property shown in Section 3.2.2, we claim that the proposed consistent and stable scheme is convergent [24].

4.2. Investigation into the scheme anisotropy

In the analysis of the three-dimensional EM wave numerical method, the two angles ϕ and θ shown schematically in Fig. 1

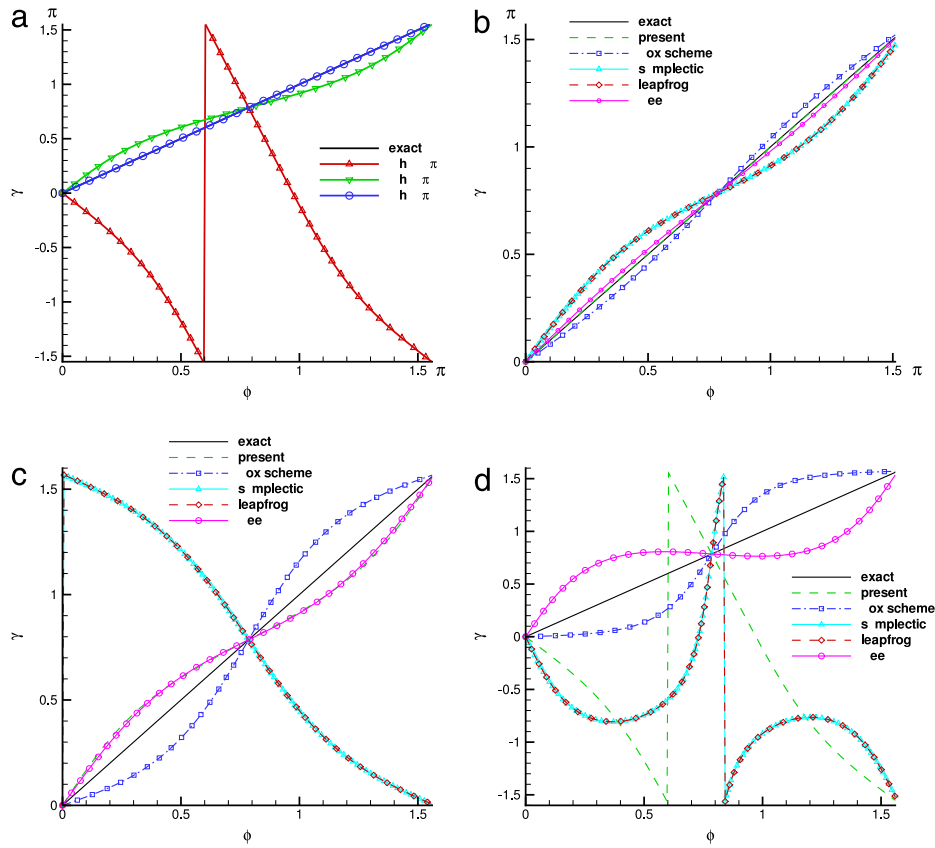


Fig. 5. The exact and numerical group velocity angles γ are plotted with respect to the wavenumber angle ϕ at different modified wavenumbers. (a) The present numerical phase velocity optimized scheme; (b) scheme comparison at $kh = \frac{\pi}{4}$; (c) scheme comparison at $kh = \frac{\pi}{2}$; (d) scheme comparison at $kh = \frac{3\pi}{4}$.

are used to express the wavenumber vector $\underline{k} = (k_x, k_y, k_z) = |k|(\sin \theta \cos \phi, \sin \theta \sin \phi, \cos \theta)$, where θ and ϕ are denoted as the zenith and azimuthal angles, respectively. The previously derived numerical dispersion relation equation can be rewritten in terms of the polar coordinates as follows

$$\begin{aligned} \sin^2(\omega_{num} \Delta t / 2) = & Cr_x^2 (a_1 \sin(3k \sin \theta \cos \phi \Delta x) \\ & + a_2 \sin(2k \sin \theta \cos \phi \Delta x) + a_3 \sin(k \sin \theta \cos \phi \Delta x))^2 \\ & + Cr_y^2 (a_1 \sin(3k \sin \theta \sin \phi \Delta y) + a_2 \sin(2k \sin \theta \sin \phi \Delta y) \\ & + a_3 \sin(k \sin \theta \sin \phi \Delta y))^2 \\ & + Cr_z^2 (a_1 \sin(3k \cos \theta \Delta z) + a_2 \sin(2k \cos \theta \Delta z) \\ & + a_3 \sin(k \cos \theta \Delta z))^2. \end{aligned} \quad (25)$$

The above equation shows that the numerical angular frequency ω_{num} varies with the angle of wavenumber vector and the Courant numbers $Cr_x (\equiv \frac{c\Delta t}{\Delta x})$, $Cr_y (\equiv \frac{c\Delta t}{\Delta y})$ and $Cr_z (\equiv \frac{c\Delta t}{\Delta z})$.

We set $\theta = \pi/2$ to simplify the anisotropy analysis. This angle is then substituted into the dispersion relation equation that accounts for the numerical angular frequency. Both of the exact and numerical angular frequencies are plotted with respect to k_x and k_y in Fig. 2(a) and (b) within the two-dimensional context for simplicity. In Fig. 2(c)–(e), one can see that the numerical dispersion surface ω_{num} is equal to that of the exact dispersion near the origin of $\underline{k} = (k_x, k_y) = |k|(\cos \phi, \sin \phi)$, where $\phi = \tan^{-1} \left(\frac{k_y}{k_x} \right)$ is shown schematically in Fig. 1(a). As the wavenumber is further away from the origin of (k_x, k_y) plane, the observed discrepancy between the numerical and the exact angular frequencies indicates the occurrence of unphysical waves in the numerical solutions [25]. The contours of ω_{num} are also

plotted with respect to k_x and k_y in Fig. 2(f). For the sake of comparison, the numerical angular frequencies of the proposed scheme and the other four schemes are plotted with respect to k_x and k_y in Fig. 3. The error contours of the schemes are compared in Fig. 4.

We also derive the numerical group velocity optimized scheme from Eq. (25). The wave solution predicted from the proposed scheme with its numerical group velocity depends not only on the magnitude of the wavenumber vector \underline{k} , or $|\underline{k}|$, but also on the direction of wavenumber vector \underline{k} , or $\tan^{-1} \left(\frac{k_y}{k_x} \right)$. The numerical error related to the derived grid-anisotropy [19] causes the predicted wave propagating not only at an incorrect velocity but also in a wrong direction. To get a better understanding of the anisotropy error, we consider, for example, a plane wave propagating along a direction, which has the unit vector $(\sin \theta' \cos \phi', \sin \theta' \sin \phi', \cos \theta')$ in the spherical coordinate system (r, θ', ϕ') , in the following error analysis.

Within the two-dimensional context, the angle of group velocity vector can be expressed by a single angle, which is γ schematically shown in Fig. 1(b). The numerical group velocity derived in the two-dimensional domain can then be expressed as

$$\underline{v}_g \left(\equiv \frac{\partial \omega_{num}}{\partial \underline{k}} \right) = |\underline{v}_g|(\cos \gamma, \sin \gamma), \text{ where } \gamma = \tan^{-1} \left(\frac{(v_g)_y}{(v_g)_x} \right).$$

The exact and numerical group velocity angles γ are then plotted with respect to the wavenumber angle ϕ in Fig. 5. One can clearly find that in the low modified wavenumber regime, the predicted angle of group velocity agrees very well with the angle of exact wavenumber vector, which is $\frac{\pi}{4}$ as shown in Fig. 3(a). With an increased value of kh , the resulting discrepancy between the exact, which is $\frac{\gamma}{\phi} = 1$, and the predicted ratio of $\frac{\gamma}{\phi}$ increases accordingly.

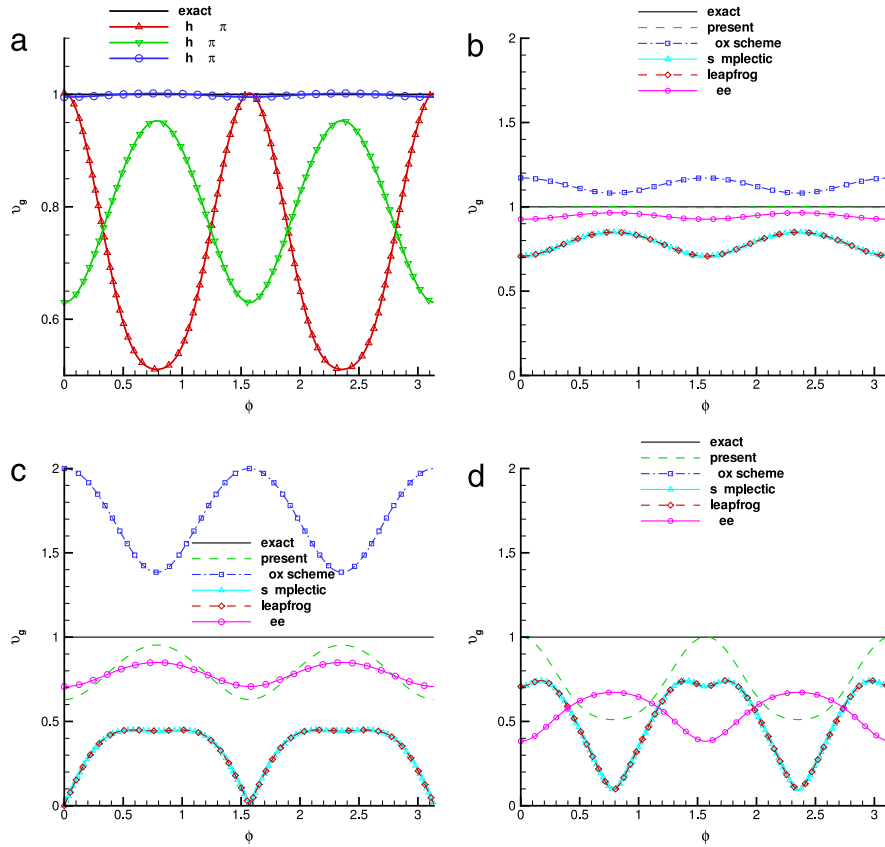


Fig. 6. The exact and numerical group velocity magnitudes are plotted with respect to the wavenumber angle ϕ at different modified wavenumbers. (a) the present numerical phase velocity optimized scheme; (b) scheme comparison at $kh = \frac{\pi}{4}$; (c) scheme comparison at $kh = \frac{\pi}{2}$; (d) scheme comparison at $kh = \frac{3\pi}{4}$.

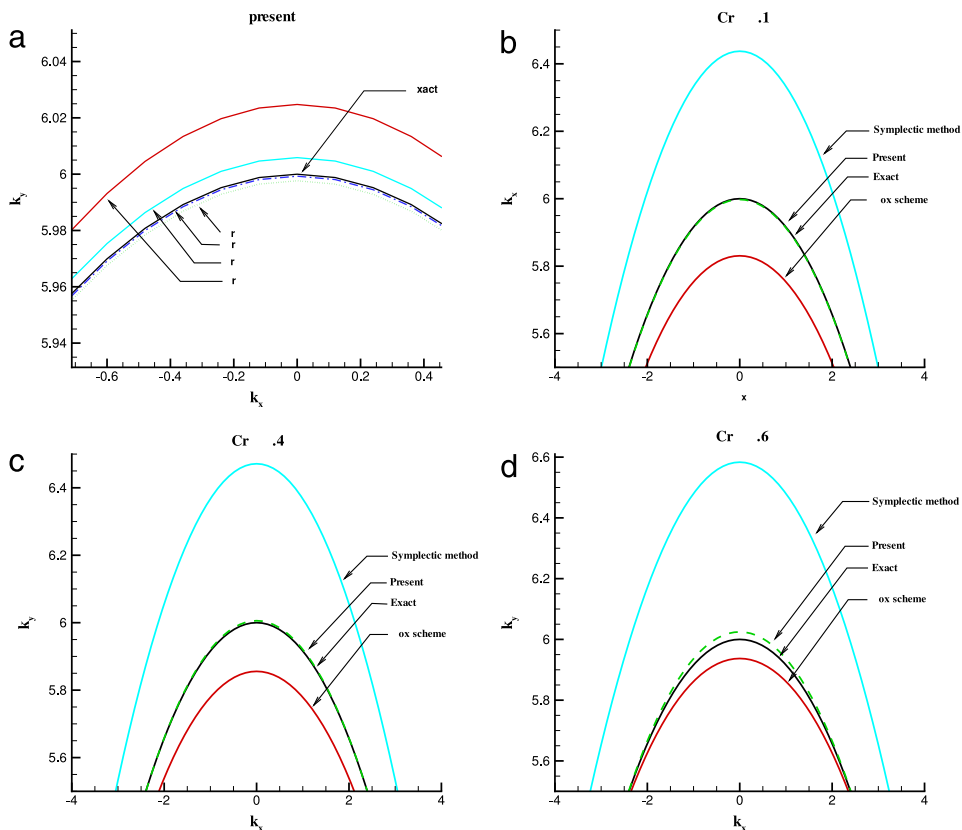


Fig. 7. The contours of $\omega_{num} = 6$ are plotted with respect to k_x and k_y at different values of the Courant number for different schemes. (a) $Cr = 0.1, 0.2, 0.4, 0.6$; (b) $Cr = 0.1$; (c) $Cr = 0.4$; (d) $Cr = 0.6$.

Table 3

The dispersion relation equations and their spatial orders of accuracy for the proposed and other four schemes. Schemes 1, 2, 3, 4, 5 denote the current, box [11], symplectic [11], leapfrog [11], and Yee [2] schemes, respectively. The exact dispersion relation equation is also shown in this table.

	Dispersion relation equation	Spatial accuracy order
1	$\frac{\omega^2}{4c^2} \left(\frac{\sin(\omega\Delta t/2)}{\omega\Delta t} \right)^2 = k_x^2 \left(3a_1 \frac{\sin(3k_x\Delta x)}{3k_x\Delta x} + 2a_2 \frac{\sin(2k_x\Delta x)}{2k_x\Delta x} + a_3 \frac{\sin(k_x\Delta x)}{k_x\Delta x} \right)^2$ $+ k_y^2 \left(3a_1 \frac{\sin(3k_y\Delta y)}{3k_y\Delta y} + 2a_2 \frac{\sin(2k_y\Delta y)}{2k_y\Delta y} + a_3 \frac{\sin(k_y\Delta y)}{k_y\Delta y} \right)^2$ $+ k_z^2 \left(3a_1 \frac{\sin(3k_z\Delta z)}{3k_z\Delta z} + 2a_2 \frac{\sin(2k_z\Delta z)}{2k_z\Delta z} + a_3 \frac{\sin(k_z\Delta z)}{k_z\Delta z} \right)^2$	4
2	$\frac{\tan^2(\frac{1}{2}\omega\Delta t)}{c^2\Delta t^2} = \frac{\tan^2(\frac{1}{2}k_x\Delta x)}{\Delta x^2} + \frac{\tan^2(\frac{1}{2}k_y\Delta y)}{\Delta y^2}$	2
3	$4 \frac{\tan^2(\frac{1}{2}\omega\Delta t)}{c^2\Delta t^2} = \frac{\sin^2(k_x\Delta x)}{\Delta x^2} + \frac{\sin^2(k_y\Delta y)}{\Delta y^2}$	2
4	$\frac{\sin^2(\omega\Delta t)}{c^2\Delta t^2} = \frac{\sin^2(k_x\Delta x)}{\Delta x^2} + \frac{\sin^2(k_y\Delta y)}{\Delta y^2}$	2
5	$\frac{\sin^2(\frac{1}{2}\omega\Delta t)}{c^2\Delta t^2} = \frac{\sin^2(\frac{1}{2}k_x\Delta x)}{\Delta x^2} + \frac{\sin^2(\frac{1}{2}k_y\Delta y)}{\Delta y^2}$ $\frac{\omega^2}{c^2} = k_x^2 + k_y^2 \text{ (exact)}$	2

Table 4

The coefficients a_1 , a_2 and a_3 in the proposed three dimensional scheme.

	$\theta = 0^\circ, 180^\circ$	$\theta = 30^\circ, 150^\circ$	$\theta = 45^\circ, 135^\circ$	$\theta = 60^\circ, 120^\circ$	$\theta = 90^\circ$
$\phi = 0^\circ, 90^\circ$ $= 180^\circ, 270^\circ$	$a_1 = 0.023854$ $a_2 = -0.17792$ $a_3 = 0.784271$	$a_1 = 0.020878$ $a_2 = -0.166014$ $a_3 = 0.769392$	$a_1 = 0.018315$ $a_2 = -0.15576$ $a_3 = 0.756574$	$a_1 = 0.020878$ $a_2 = -0.166014$ $a_3 = 0.769392$	$a_1 = 0.023854$ $a_2 = -0.177916$ $a_3 = 0.784271$
$\phi = 6^\circ, 84^\circ$ $= 96^\circ, 174^\circ$ $= 186^\circ, 264^\circ$ $= 276^\circ, 354^\circ$	$a_1 = 0.023743$ $a_2 = -0.177471$ $a_3 = 0.7837133$	$a_1 = 0.020766$ $a_2 = -0.165564$ $a_3 = 0.76883$	$a_1 = 0.0182556$ $a_2 = -0.155522$ $a_3 = 0.756278$	$a_1 = 0.020879$ $a_2 = -0.166017$ $a_3 = 0.769397$	$a_1 = 0.023854$ $a_2 = -0.177916$ $a_3 = 0.784271$
$\phi = 9^\circ, 81^\circ$ $= 99^\circ, 171^\circ$ $= 189^\circ, 261^\circ$ $= 279^\circ, 351^\circ$	$a_1 = 0.023603$ $a_2 = -0.176912$ $a_3 = 0.783015$	$a_1 = 0.0206242$ $a_2 = -0.164997$ $a_3 = 0.7681209$	$a_1 = 0.0181826$ $a_2 = -0.15523$ $a_3 = 0.755913$	$a_1 = 0.02088$ $a_2 = -0.1660218$ $a_3 = 0.769402$	$a_1 = 0.023854$ $a_2 = -0.177916$ $a_3 = 0.784271$
$\phi = 12^\circ, 78^\circ$ $= 102^\circ, 168^\circ$ $= 192^\circ, 258^\circ$ $= 282^\circ, 348^\circ$	$a_1 = 0.023406$ $a_2 = -0.176126$ $a_3 = 0.7820323$	$a_1 = 0.020423$ $a_2 = -0.164194$ $a_3 = 0.767117$	$a_1 = 0.018082$ $a_2 = -0.154829$ $a_3 = 0.755411$	$a_1 = 0.020882$ $a_2 = -0.166028$ $a_3 = 0.769411$	$a_1 = 0.023854$ $a_2 = -0.177916$ $a_3 = 0.784271$
$\phi = 22.5^\circ, 67.5^\circ$ $= 112.5^\circ, 157.5^\circ$ $= 202.5^\circ, 247.5^\circ$ $= 292.5^\circ, 337.5^\circ$	$a_1 = 0.022238$ $a_2 = -0.171452$ $a_3 = 0.77619$	$a_1 = 0.0192028$ $a_2 = -0.1593112$ $a_3 = 0.761014$	$a_1 = 0.0175488$ $a_2 = -0.1526952$ $a_3 = 0.752744$	$a_1 = 0.0208917$ $a_2 = -0.166067$ $a_3 = 0.769459$	$a_1 = 0.023854$ $a_2 = -0.177916$ $a_3 = 0.784271$
$\phi = 30^\circ, 60^\circ$ $= 120^\circ, 150^\circ$ $= 210^\circ, 240^\circ$ $= 300^\circ, 330^\circ$	$a_1 = 0.020878$ $a_2 = -0.16601$ $a_3 = 0.76939$	$a_1 = 0.017748$ $a_2 = -0.153492$ $a_3 = 0.753740$	$a_1 = 0.0170712$ $a_2 = -0.150785$ $a_3 = 0.750356$	$a_1 = 0.0209008$ $a_2 = -0.166103$ $a_3 = 0.7695043$	$a_1 = 0.023854$ $a_2 = -0.177916$ $a_3 = 0.784271$
$\phi = 36^\circ, 54^\circ$ $= 126^\circ, 144^\circ$ $= 216^\circ, 234^\circ$ $= 306^\circ, 324^\circ$	$a_1 = 0.019542$ $a_2 = -0.160668$ $a_3 = 0.76271$	$a_1 = 0.016313$ $a_2 = -0.14775$ $a_3 = 0.746566$	$a_1 = 0.016727$ $a_2 = -0.149407$ $a_3 = 0.748634$	$a_1 = 0.020907$ $a_2 = -0.166129$ $a_3 = 0.769537$	$a_1 = 0.023854$ $a_2 = -0.177916$ $a_3 = 0.784271$
$\phi = 45^\circ, 135^\circ$ $= 225^\circ, 315^\circ$	$a_1 = 0.018314$ $a_2 = -0.15576$ $a_3 = 0.75657$	$a_1 = 0.015007$ $a_2 = -0.14253$ $a_3 = 0.740037$	$a_1 = 0.016489$ $a_2 = -0.148457$ $a_3 = 0.747446$	$a_1 = 0.0209117$ $a_2 = -0.166147$ $a_3 = 0.769558$	$a_1 = 0.023854$ $a_2 = -0.177916$ $a_3 = 0.784271$

Indeed, this fact has shedded some light on the generation of dispersion errors in higher wavenumber regime. The exact and numerical group velocity magnitudes are also plotted against the wavenumber angle as shown in Fig. 6. The contour values predicted at different Courant numbers are plotted as well in Fig. 7 for $\omega = 6$. The contour values for $\omega = 6, 12$ and 16 are plotted in Fig. 8 for the proposed numerical phase velocity optimized scheme. One can see that the predicted and exact solutions have no difference provided that the magnitude of ω is less than 12. Based on the

results tabulated in Table 3, the numerical accuracy is improved by using the proposed scheme.

By taking all the EM wave propagation directions into account, the error between the numerical and exact phase velocities, defined as $1 - \frac{|u_p(\omega, \theta', \phi')|}{(\mu\epsilon)^{1/2}}$, is evaluated in the three-dimensional context. Towards this perspective, in the spherical coordinate system we integrate the phase velocity error over a differential area $r^2 \sin \theta' d\theta' d\phi'$. The resulting error per spherical area $4\pi r^2$ can

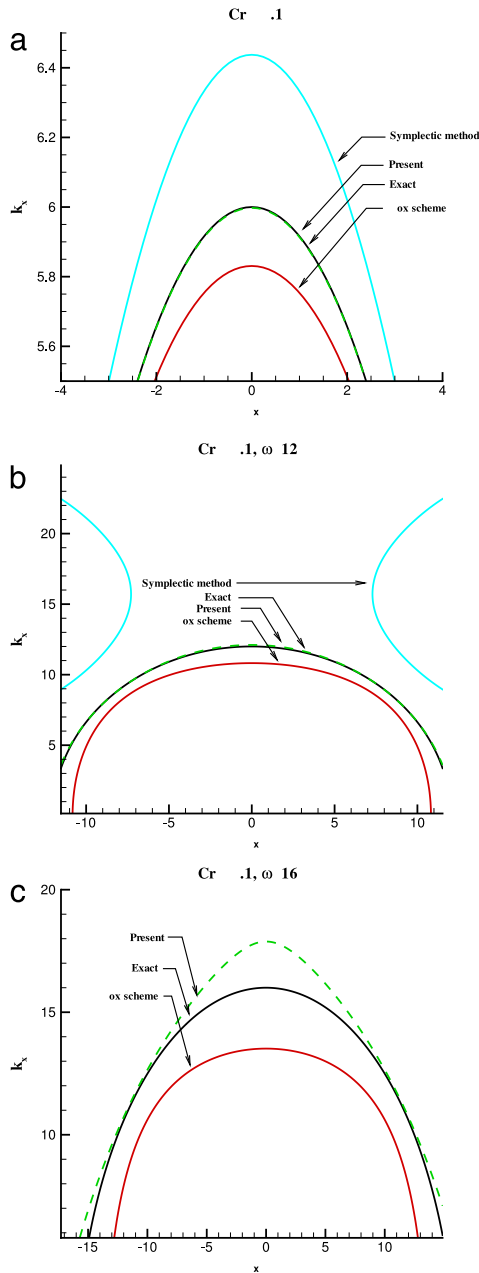


Fig. 8. Plot of the exact and numerical angular frequencies with respect to k_x and k_x at different angular frequencies for the case investigated at $Cr = 0.1$. (a) $\omega = 6$; (b) $\omega = 12$; (c) $\omega = 16$.

be computed from the definition given below

$$E_{3D}(\omega) = \frac{1}{4\pi} \int_0^\pi \int_0^{2\pi} 1 - \frac{|\underline{U}_p(\omega, \theta', \phi')|}{(\mu\varepsilon)^{1/2}} \sin \theta' d\theta' d\phi'. \quad (26)$$

The errors are plotted accordingly in Fig. 9.

According to the three derived algebraic equations in (11), (12) and (20), the introduced coefficients a_1 , a_2 and a_3 are plotted with respect to the wavenumber angle $\phi \equiv \tan^{-1} \left(\frac{k_y}{k_x} \right)$ in Fig. 10. The coefficients a_1 , a_2 and a_3 obtained at each point in the domain can then be interpolated through the data shown in Table 4 or plotted in Fig. 10. The reference characteristic speeds $c \sin \gamma$ and $c \cos \gamma$, where c is the speed of light and γ is the angle of phase velocity vector, differ from each other on a pointwise basis. At each spatial location we can then compute its local Courant numbers Cr_x and Cr_y

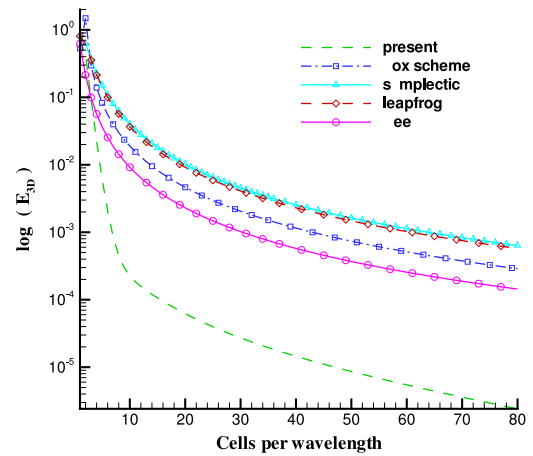


Fig. 9. The values of E_{3D} are plotted with respect to the number of cells per wavelength N_x using the proposed numerical phase velocity optimized scheme.

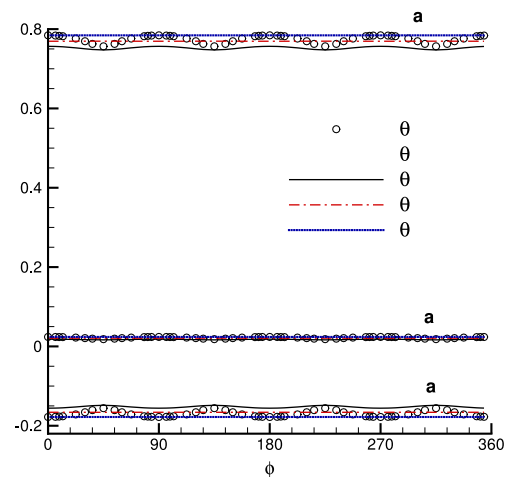


Fig. 10. The derived weighting coefficients a_1 , a_2 and a_3 are plotted with respect to the angle $\phi \equiv \tan^{-1} \left(\frac{k_y}{k_x} \right)$ at different zenith angles θ at $Cr = (Cr_x^2 + Cr_y^2 + Cr_z^2)^{1/2} = 0.2$.

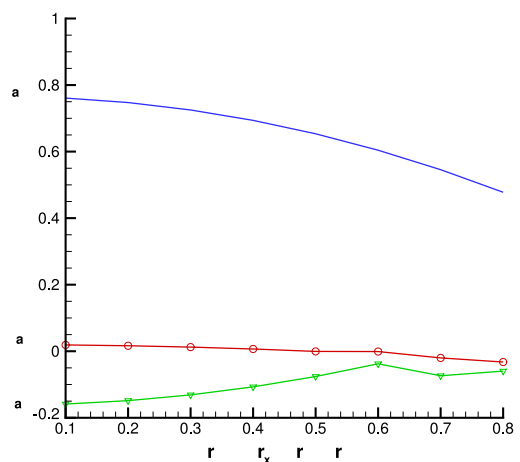


Fig. 11. The values of a_1 , a_2 and a_3 are plotted with respect to the magnitude of the Courant number $Cr = (Cr_x^2 + Cr_y^2 + Cr_z^2)^{1/2}$ ranging from 0.1 to 0.8 using the proposed numerical phase velocity optimized scheme at $\theta = \phi = \frac{\pi}{4}$.

and hence the corresponding interpolated weighting coefficients from the coefficients a_1 , a_2 and a_3 are plotted in Fig. 11.

Given the definition of $k^2 = k_x^2 + k_y^2$, the wavenumber components can be expressed as $k_x = k \cos \phi$ and $k_y = k \sin \phi$.

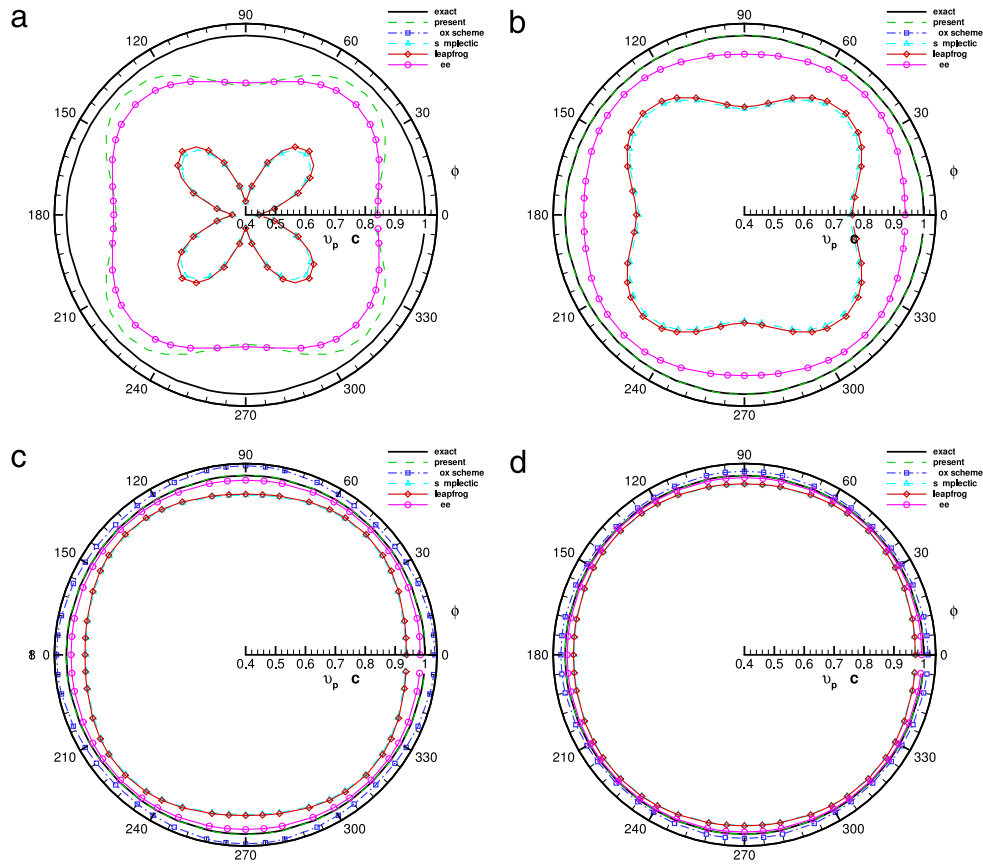


Fig. 12. Comparison of the phase velocity ratios $\frac{v_p}{c}$ versus θ at different values of N_λ using the CN [21], FDTDII [21], and the currently proposed schemes. (a) $N_\lambda = 3.1$; (b) $N_\lambda = 5$; (c) $N_\lambda = 10$; (d) $N_\lambda = 20$.

For a better presentation of the results, two extra parameters are defined. The first one is $N_\lambda = \frac{\lambda}{h}$, which denotes the number of points per wavelength λ ($= \frac{2\pi}{k}$). The second parameter is the CFL number $Cr = \frac{c\Delta t}{h}$. The speed of light c is chosen as the reference speed and $h = \Delta x = \Delta y$ is the uniform grid spacing. Given these definitions, the numerical phase velocity v_p , which is the ratio of the numerical angular frequency and the wavenumber k , can be derived. We can express $e^{i\omega_{num}\Delta t}$ by the virtue of Eq. (17) to get $e^{i\omega\Delta t} = e^{-\omega_I\Delta t}(\cos(\omega_R\Delta t) + I\sin(\omega_R\Delta t))$. Define $\hat{R} = e^{-\omega_I\Delta t}\cos(\omega_R\Delta t)$ and $\hat{I} = e^{-\omega_I\Delta t}\sin(\omega_R\Delta t)$, the value of $\tan(\omega_R\Delta t) = \frac{\hat{I}}{\hat{R}}$ and the ratio of the numerical phase velocity $|v_p| = |\frac{\omega_R}{k}|$ to the exact phase velocity c can be obtained as [26]

$$\frac{v_p}{c} = \frac{\omega_R}{ck} = \frac{N_\lambda}{2\pi Cr} \tan^{-1}\left(\frac{\hat{I}}{\hat{R}}\right). \quad (27)$$

In the current comparison study, the ratios of the derived numerical phase velocity and the exact phase velocity, which is $\frac{v_p}{c}$, are plotted at different values of N_λ for all the benchmark schemes viz. the Box scheme, the symplectic scheme, the leapfrog scheme, and the Yee's scheme in Fig. 12. For the simulation case with fewer grid points per wavelength, our scheme has been shown to have a more accurate prediction of phase velocity. Also, the proposed dispersion-error reducing scheme performs better near the angle $\phi = 45^\circ$. By increasing the value of N_λ , the numerical phase velocity approaches the exact phase velocity asymptotically. In addition, it is obvious that the dispersion relation equation of the present scheme has the best agreement with the exact dispersion relation equation as shown in Fig. 4.

Table 5

The predicted spatial rates of convergence (sroc) for the analytic test problem in Section 6.1.

Meshes	L_2 -error norm of E_z	sroc
$10 \times 10 \times 10$	1.8366E-05	–
$20 \times 20 \times 20$	1.2339E-06	3.8957
$30 \times 30 \times 30$	8.5169E-08	3.8567
$40 \times 40 \times 40$	5.3609E-09	3.9897

5. Absorbing boundary condition

Constitutive equations $\underline{B} = [\mu^*] \underline{H}$ and $\underline{D} = [\epsilon^*] \underline{E}$ are applied to describe the response of optical media to the electromagnetic field. Two tensors $[\mu^*]$ and $[\epsilon^*]$ are generally defined as $[\epsilon^*] = [\epsilon] + \frac{[\sigma_E]}{I\omega}$ and $[\mu^*] = [\mu] + \frac{[\sigma_M]}{I\omega}$, where $[\sigma_E]$ and $[\sigma_M]$ are denoted as the electric conductivity and magnetic conductivity tensors, respectively. The impedance of the chosen UPML (Uniaxial Perfectly Matched Layer) should match with that in free space by $\epsilon_0^{-1}\mu_0 = [\epsilon^*]^{-1}[\mu^*]$. Near the boundary of a scatter field, the attached absorbing layer for the mitigation of spurious wave reflections is characterized by the constitutive equation given by $[S] = [S]_x[S]_y[S]_z = \frac{[\epsilon^*]}{\epsilon_0} = \frac{[\mu^*]}{\mu_0}$ to attenuate the electromagnetic wave along x, y, z directions, respectively, through the diagonal tensors. The components of these constitutive tensors are represented by $s_{\alpha(\alpha=x,y,z)} = 1 + \frac{\sigma_{max}|\alpha-\alpha_0|^n}{I\omega\epsilon_0\delta^n}$ [27], where δ denotes the depth of UPML. The value of n appeared in the conductivity profile $\frac{\sigma_{max}|\alpha-\alpha_0|^n}{\delta^n}$ is set at 3. Based on the results predicted on the $121 \times 121 \times 121$ uniformly distributed nodes, this chosen value gives the best absorption performance in UPML as shown in Fig. 13. The location at which α equals to α_0 is the interface between the

Table 6
Comparison of the required CPU times for the present scheme with the optimized phase velocity and the Yee's scheme given in [2], which yield approximately the same L_2 -error norm, at time $t = 10$.

Present			Yee [2]		
L_2 -error norm	Grid	CPU time (s)	L_2 -error norm	Grid	CPU time (s)
8.7962E-03	41 × 41	0.1092	8.3483E-03	181 × 181	4.9608
4.0657E-03	51 × 51	0.2028	4.8228E-03	251 × 251	13.0261
2.0981E-03	61 × 61	0.3276	3.0141E-03	341 × 341	33.0092

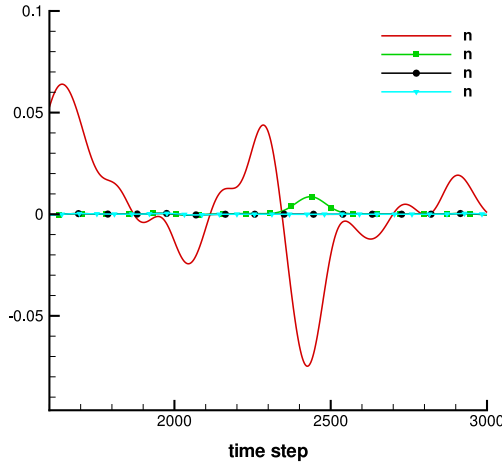


Fig. 13. Comparison of the values of $E_z(t)$ at the point P ($x = 336$ nm, $y = 0$ nm, $z = 336$ nm) for the different magnitudes of n shown in the conductivity profile $\frac{\sigma_{max}|e^{-\sigma_0}|^n}{\delta^n}$ using the proposed scheme.

UPML and the scatter field. In the constitutive tensor, σ_{max} is chosen as $\frac{(n+1)\ln(1/R_0)}{2\delta}$ [27], where $1/R_0 = 10^{16}$.

6. Numerical results

6.1. Verification studies

The explicit symplectic PRK scheme endowed with the optimized numerical phase velocity derived in non-staggered grids is verified by solving the three-dimensional Maxwell's equations with analytic solution. In $-\pi \leq x \leq \pi$, $-\pi \leq y \leq \pi$ and $-\pi \leq z \leq \pi$, the solutions of the Maxwell's equations sought at $\mu = 1$ and $\varepsilon = 1$ are subjected to the initial solenoidal solutions

$$\begin{aligned} E_x(x, y, z, 0) &= E_y(x, y, z, 0) = E_z(x, y, z, 0) = 0, \\ H_x(x, y, z, 0) &= \cos(x + y + z), \\ H_y(x, y, z, 0) &= \frac{1}{2}(-1 + \sqrt{3}) \cos(x + y + z), \\ H_z(x, y, z, 0) &= -\frac{1}{2}(1 + \sqrt{3}) \cos(x + y + z). \end{aligned} \quad (28)$$

The exact electric and magnetic field solutions of Eqs. (1)–(2) are given as

$$\begin{aligned} E_x(x, y, z, t) &= \sin(\sqrt{3}t) \sin(x + y + z), \\ E_y(x, y, z, t) &= -\frac{1}{2}(1 + \sqrt{3}) \sin(\sqrt{3}t) \sin(x + y + z), \\ E_z(x, y, z, t) &= \frac{1}{2}(-1 + \sqrt{3}) \sin(\sqrt{3}t) \sin(x + y + z), \\ H_x(x, y, z, t) &= \cos(\sqrt{3}t) \cos(x + y + z), \\ H_y(x, y, z, t) &= \frac{1}{2}(-1 + \sqrt{3}) \cos(\sqrt{3}t) \cos(x + y + z), \\ H_z(x, y, z, t) &= -\frac{1}{2}(1 + \sqrt{3}) \cos(\sqrt{3}t) \cos(x + y + z). \end{aligned} \quad (29)$$

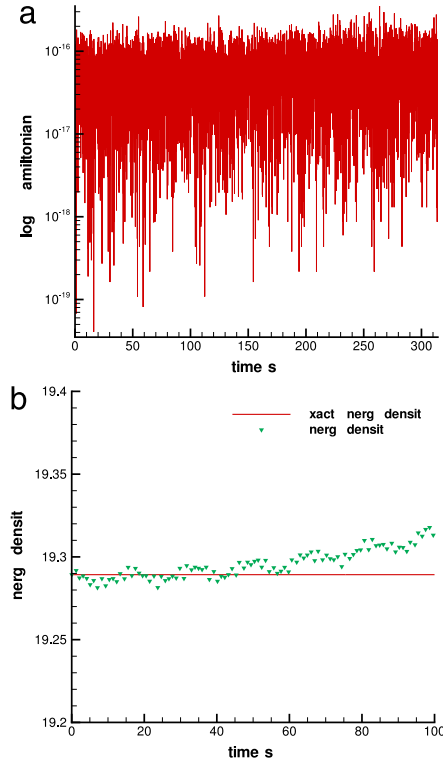


Fig. 14. Comparison of the computed and exact energy densities, shown in (3)–(4), with respect to time for the analytical problem using the proposed dispersion optimized scheme. (a) Hamiltonian function; (b) Energy density.

In order to obtain the spatial rate of convergence, all the calculations are carried out at $\Delta t = 10^{-5}$, which is much smaller than the four chosen grid spacings $\Delta x = \Delta y = \Delta z = 2\pi/5, 2\pi/10, 2\pi/20$ and $2\pi/40$. The tabulated L_2 -error norms in Table 5 show that the predicted spatial rate of convergence deviates slightly from the theoretical order of accuracy (i.e. 4).

The Hamiltonian defined in (3) and the energy density given in (4) are calculated for making an indirect justification on the proposed scheme. Fig. 14 shows clearly that the computed values of Hamiltonian and energy density are well conserved as time elapses. The time-varying L_2 -norms of the scalars $\nabla \cdot \underline{H}$ and $\nabla \cdot \underline{E}$ are plotted to examine if Gauss's law is satisfied discretely. In Fig. 15, the predicted magnetic and electric fields are almost divergence-free. We also assess the currently proposed scheme with other four schemes in terms of the required CPU times for attaining the same L_2 -error norm. The results shown in Table 6 explain why we employ the proposed scheme to compute the solution of Maxwell's equations.

6.2. Mie scattering problem

The Mie scattering wave propagation is then investigated in a three-dimensional domain $\Omega = (-380 \text{ nm} \leq x, y, z \leq 380 \text{ nm})$. The diameter of the investigated dielectric cylinder is 126.56 nm and it is located at the center of a cube. This isotropic cylinder in

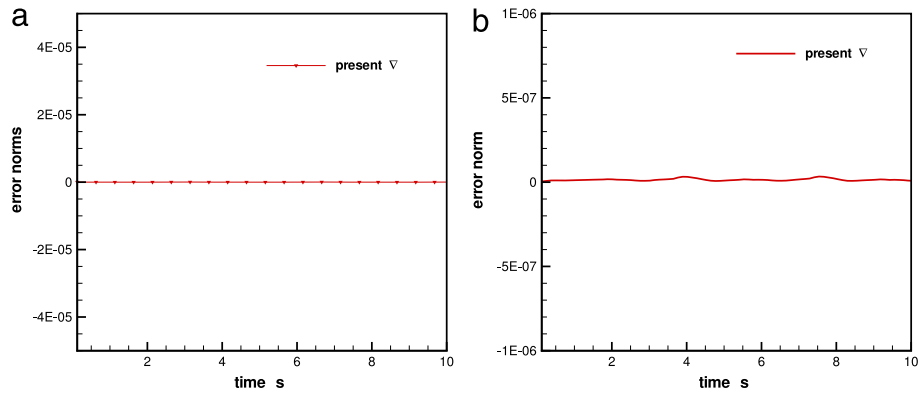


Fig. 15. Plot of the computed L_2 -norms of $\nabla \cdot H$ and $\nabla \cdot E$ by the proposed spatial scheme with respect to time using the fourth-order Runge–Kutta scheme and the present explicit partitioned Runge–Kutta symplectic scheme (a) $\nabla \cdot H$; (b) $\nabla \cdot E$.

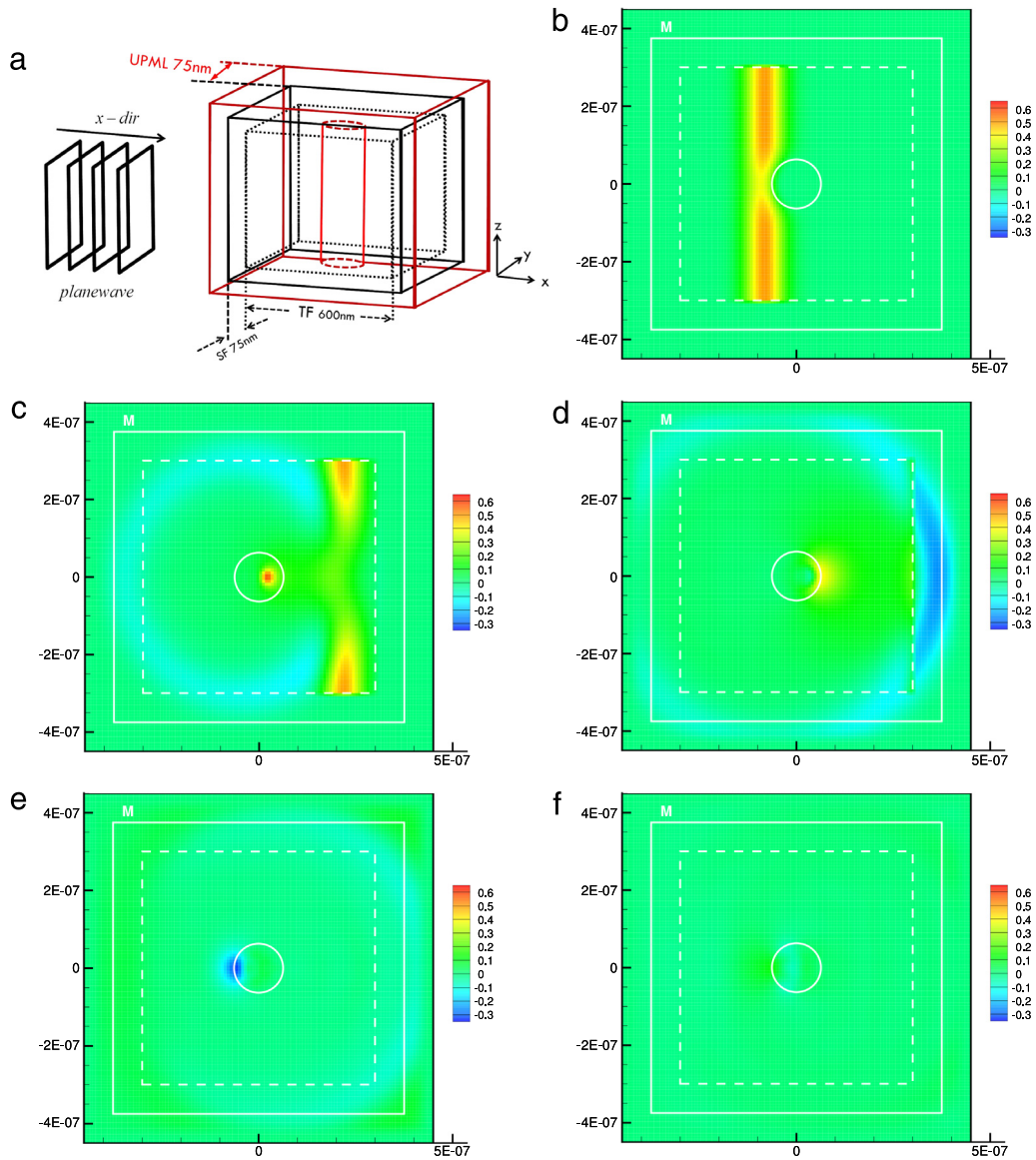


Fig. 16. The predicted contours of E_z ($z = 0$) at the cutting plane containing a cylindrical scatterer. (a) Schematic of the 3D Mie scattering problem; (b) timestep = 560 (2.8 fs); (c) timestep = 760 (3.8 fs); (d) timestep = 1350 (4.25 fs); (e) timestep = 1600 (5.8 fs); (f) timestep = 1900 (9 fs).

the homogeneous air medium has $\epsilon_r = 12.1104$. The incident x -polarized plane wave with the amplitude of $0.5 \frac{V}{m}$ and the angular frequency of $13.263 \frac{rad}{s}$ propagates towards the positive x -direction.

The Mie scattering problem is then investigated in a cube with the cross-section area of $760 \times 760 \text{ nm}^2$. For the case of one dielectric cylinder, the incident wave is scattered so that the total field/scattered field formulation is adopted. The physical domain

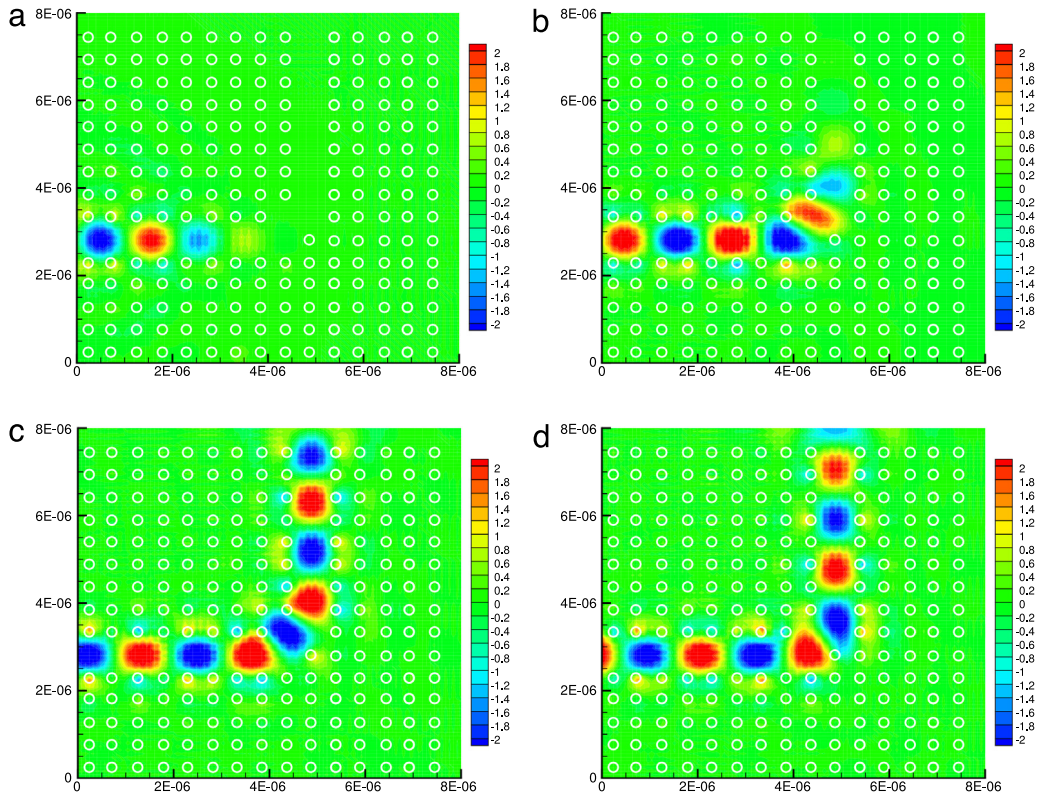


Fig. 17. The predicted E_z ($z = 0$) contours at the cutting plane. (a) timestep = 575 (30.68775 fs); (b) timestep = 1075 (57.37275 fs); (c) timestep = 1750 (93.3975 fs); (d) timestep = 2325 (124.08525 fs).

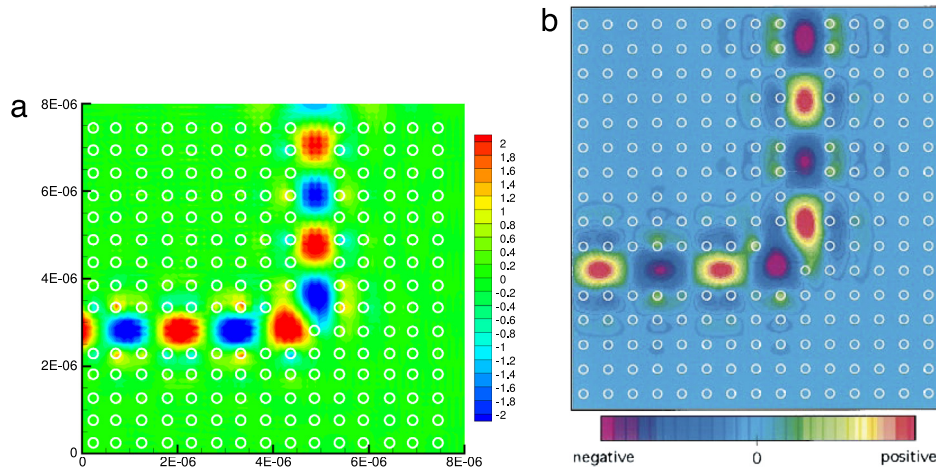


Fig. 18. The computed E_z field values at the time step 2325 (or $t = 124.08525$ fs) in the PC-based L-shape waveguide at the normalized frequency $0.353(c/a)$. (a) Present; (b) Mekis et al. [22].

containing 121 nodal points along each spatial direction is divided into three regions. The total field composes the investigated dielectric cylinder whereas the region of scattered field encloses the region of the total field. The scattered field components are stored only in the scattered field.

The problem under investigation is the EM wave scattered from a cylindrically-shaped scatter located at the center of the physical domain schematically shown in Fig. 16(a). This problem is chosen for investigating the three-dimensional effect on the EM wave propagation. The results are calculated at the same Courant number $Cr = 0.2$, which corresponds to the specified time increment $\Delta t = 0.0026685$ fs. The three-dimensional results for E_z are plotted in Fig. 16(b)–(f) at the cutting plane $z = 0$ nm.

6.3. Photonic crystal L-shaped bent waveguide problem

A lattice of finite-length vertical rods (dielectric pillars) is considered in a domain defined in $0 \leq x, y, z \leq 8000$ nm containing a L-shaped defect channel. The relative permittivity of the medium surrounding the uniformly distributed pillars is set at 1. The dielectric constant of these pillars is assumed to be $\epsilon_r = 11.56$. The waveguide of width $\frac{w}{a} = 2$ is constructed by taking one pair of the vertical and row pillars away from the original uniformly distributed lattice. A light with the frequency belonging to the photonic band gap is confined in this three-dimensional L-shaped defect channel. A transverse magnetic wave

incident into the domain propagates from left to right. For getting a wider photonic band gap, the radius of all pillars is chosen as $0.2a$, where the lattice related constant a ($=515$ nm) denotes the length between the centroids of two adjacent pillars.

The L-shaped bent waveguide problem is simulated at $\Delta t = 0.05337$ fs and $h = 57.1429$ nm. A uniaxial perfectly matched layer enclosing the scatter field is applied to absorb the wave and avoid any re-entry of unphysical wave into the domain. Fig. 17 shows the time-evolving E_z contours computed at the normalized frequency $= 0.353$ ($\frac{c}{a}$) (or wavelength $= 1458.92$ nm), where c denotes the speed of light. The optical wave is seen to propagate through the ninety-degree bend and the electric field is concentrated mostly in this defect channel. Comparison of the current three-dimensional result in the L-shaped defect channel with the two-dimensional result of Mekis et al. [22] is illustrated in Fig. 18.

7. Conclusions

A FDTD scheme has been developed on non-staggered grids to solve the three-dimensional Maxwell's equations in isotropic, homogeneous, and non-lossy material. Our aim is to numerically preserve symplecticity and conserve helicity and quadratic Hamiltonians as computation progresses. Given the fact that Maxwell's equations correspond to a separable Hamiltonian system, the explicit partitioned Runge–Kutta symplectic time integrator is applied together with the space-centered finite difference scheme. The resulting fully discrete numerical scheme can indeed conserve the energy in the discrete level. To increase the dispersion accuracy, the difference between the numerical and the exact phase velocities is minimized. The predicted temporally second-order and spatially fourth-order accurate Maxwell's solutions have been shown to satisfy the discrete Gauss' law for the magnetic and electric fields. The current numerical solutions have shown good agreement with the exact and the benchmark numerical solutions.

Acknowledgments

This work was supported by the National Science Council of the Republic of China under the Grants NSC96-2221-E-002-293-MY2, NSC96-2221-E-002-004, and CQSE97R0066-69.

References

- [1] J.X. Cai, Y.S. Wang, B. Wang, B. Jiang, *J. Math. Phys.* 47 (2006) 1–18.
- [2] K.S. Yee, *IEEE Trans. Antennas and Propagation* 14 (1966) 302–307.
- [3] C.-D. Munz, P. Ommes, R. Schneider, E. Sonnendrücker, U. Voß, *J. Comput. Phys.* 161 (2000) 484–511.
- [4] B. Cockburn, F. Li, C.-W. Shu, *J. Comput. Phys.* 194 (2004) 588–610.
- [5] M. Lilienthal, S.M. Schnepp, T. Weiland, *J. Comput. Phys.* 275 (2014) 589–607.
- [6] H. Egger, F. Kretzschmar, S.M. Schnepp, T. Weiland, A space-time discontinuous Galerkin Trefftz method for time dependent Maxwell's equations, arXiv:1412.2637v2.
- [7] T.T. Zygidis, T.D. Tsiboukis, *J. Comput. Phys.* 226 (2007) 2372–2388.
- [8] T.J. Bridges, S. Reich, *Phys. Lett. A* 284 (2001) 184–193.
- [9] N. Anderson, A.M. Arthurs, *Int. J. Electron.* 54 (1983) 861–864.
- [10] J.E. Marsden, A. Weinstein, *Physica D* 4 (1982) 394–406.
- [11] Y. Sun, P.S.P. Tse, *J. Comput. Phys.* 230 (2011) 2076–2094.
- [12] E. Hairer, C. Lubich, G. Wanner, *Geometric Numerical Integration: Structure-preserving Algorithms for Ordinary Differential Equations*, third ed., Springer-Verlag, Berlin, 2006.
- [13] P. Pinho, M.O. Domingues, P.J.S.G. Ferreira, S.M. Gomes, A. Gomide, J.R. Pereira, *IEEE Trans. Magn.* 43 (3) (2007) 1013–1022.
- [14] Y. Liu, *J. Comput. Phys.* 124 (1996) 396–416.
- [15] C.-D. Munz, P. Ommes, R. Schneider, *Comput. Phys. Commun.* 130 (2000) 83–117.
- [16] L. Codecasa, R. Specogna, F. Trevisan, *J. Comput. Phys.* 229 (2010) 7401–7410.
- [17] J.M. Sanz-Serna, *Physica D* (1992) 293–302.
- [18] L.L. Jiang, J.F. Mao, X.L. Wu, *IEEE Trans. Magn.* 42 (8) (2006) 1991–1995.
- [19] L.N. Trefethen, *SIAM Rev.* 24 (1982) 113–136.
- [20] G.B. Whitham, *Linear and Nonlinear Waves*, John Wiley & Sons Inc., New York, 1999.
- [21] G. Sun, C.W. Trueman, *IEEE Trans. Microw. Theory* 53 (2005) 832–842.
- [22] A. Mekis, J.C. Chen, I. Kurland, S. Fan, P.R. Villeneuve, J.D. Joannopoulos, *Phys. Rev. Lett.* 77 (1996) 3787–3790.
- [23] A. Taflov, M.E. Brodwin, *IEEE T. Microw. Theory* 23 (1975) 623–630.
- [24] R.D. Richtmyer, K.W. Morton, *Difference Methods for Initial-Value Problems*, second ed., Interscience Publishers, Wiley, New York, 1967.
- [25] U.M. Ascher, R.I. McLachlan, *Appl. Numer. Math.* 48 (2004) 255–269.
- [26] L. Gao, B. Zhang, D. Liang, *J. Comput. Appl. Math.* 205 (2007) 207–230.
- [27] S.D. Gedney, *IEEE Trans. Antennas and Propagation* 44 (1996) 1630–1639.